Investigating Rotation and Anisotropic Ablation of Small Meteoroids and their Effects on Head Echo Plasma Formation via Computational Techniques

Trevor Hedges[1], Joseph Corbett Ferguson[2], Nicolas Lee[1], Sigrid Elschot[1], Glenn Sugar[1], and Meers M. Oppenheim[3]

[1]Stanford University
[2]NASA Ames Research Center
[3]Boston University

March 04, 2025

Abstract

High-power large-aperture radar instruments observe numerous meteor head echoes per minute. Head echoes result from reflections of radio waves from plasma surrounding meteoroids as they enter Earth's atmosphere. Knowledge of the spatial distribution of electrons in this plasma is essential to determining the mass loss rate of the meteor as a function of its measured radar cross-section. Prior work applies theoretical and computational methods to determine the electron density distribution, but assumes the meteoroid emits neutral particles uniformly across its surface. In this paper, a numerical surface ablation model demonstrates that meteoroid mass loss may occur preferentially in the direction facing the oncoming atmosphere. Specifically, meteoroid mass loss becomes proportional to the frontal surface area facing the freestream atmosphere in the limit of high Biot number, but remains isotropic in the limit of low Biot number. Meteoroid rotation has a small effect on the direction of ejected mass, but the effect is insignificant compared to variation in meteoroid properties that affect the Biot number. This result informs our computational meteor plasma model, in which we compare the effect of meteoroid vaporization on the plasma distribution in the limits of low versus high Biot number. The resulting electron density profiles demonstrate order-of-magnitude agreement between each other, with peak difference of 70\% immediately upstream of the meteoroid. This implies that the directional distribution of vaporizing neutrals likely does not significantly influence head echo observations, lending credence to existing work that assumes isotropic ablation.

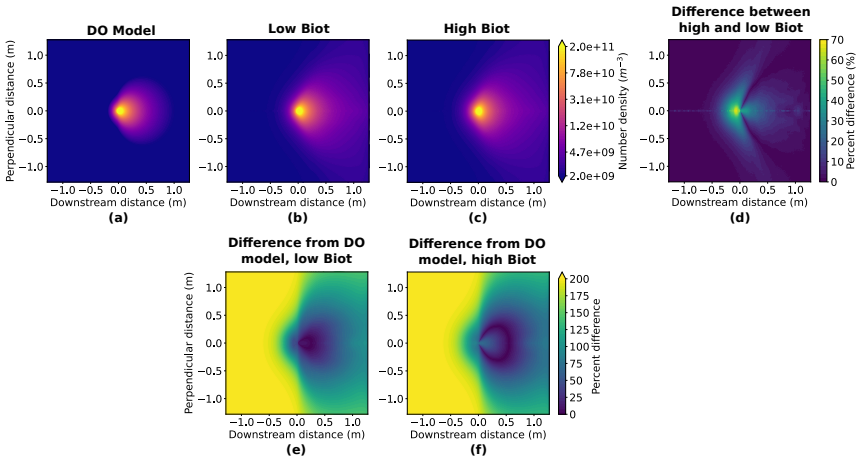

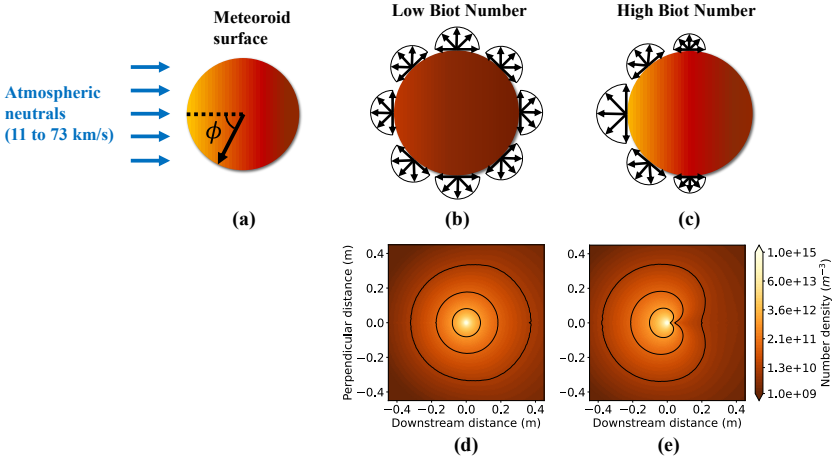

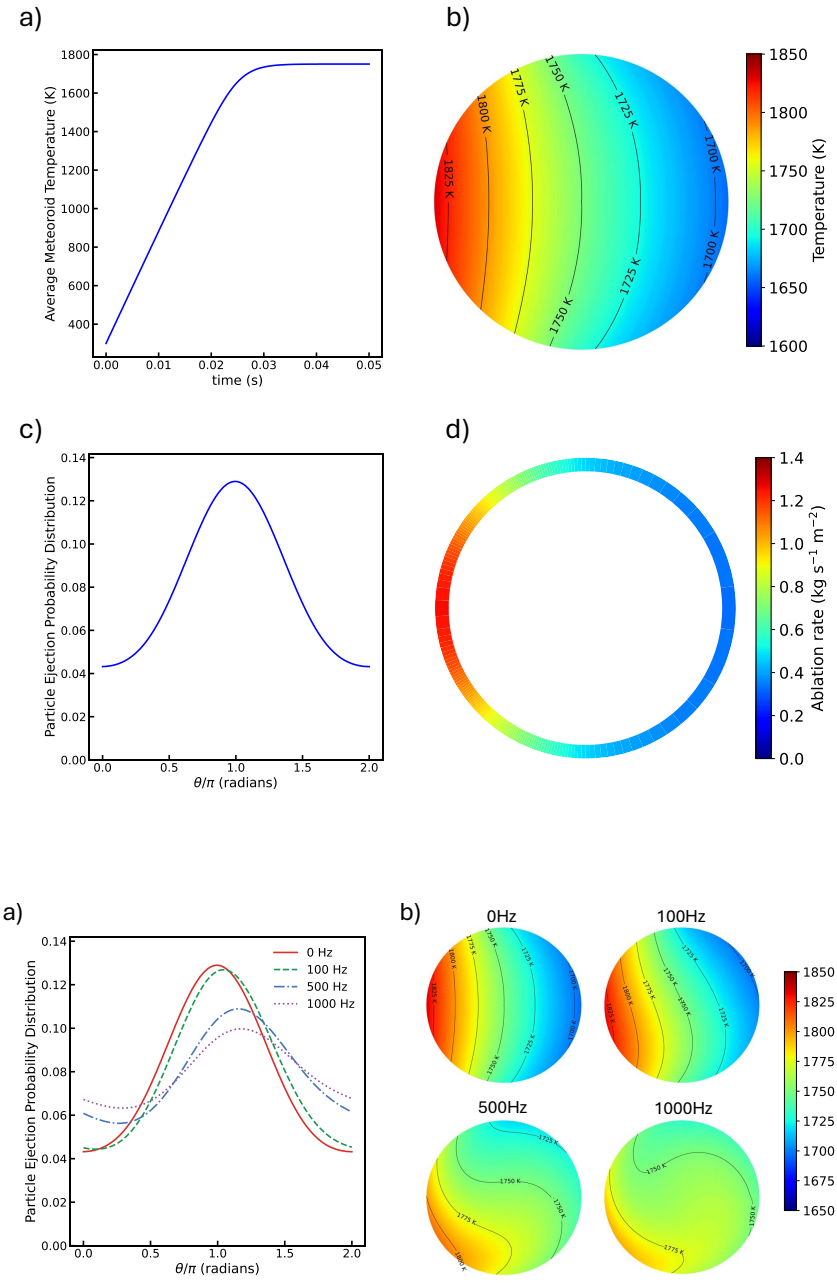

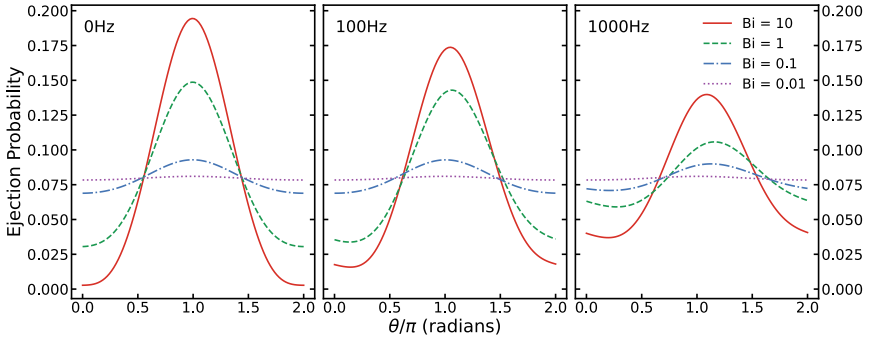

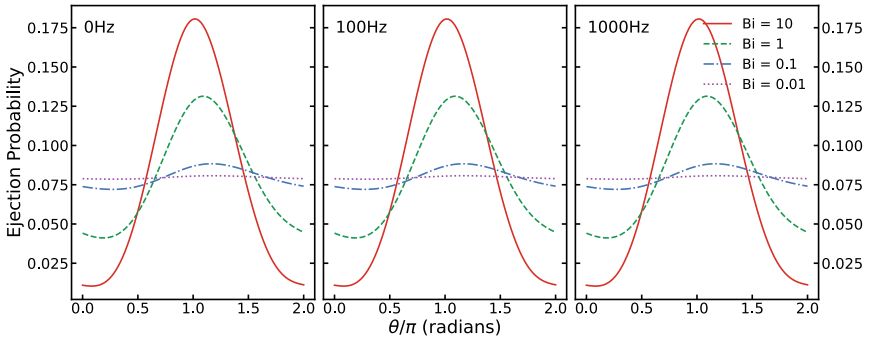

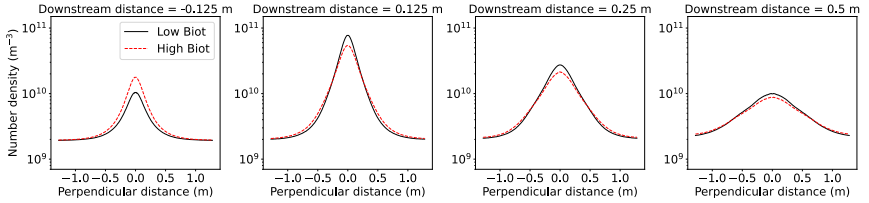

Abstract

High-power large-aperture radar instruments observe numerous meteor head echoes per minute. Head echoes result from reflections of radio waves from plasma surrounding meteoroids as they enter Earth's atmosphere. Knowledge of the spatial distribution of electrons in this plasma is essential to determining the mass loss rate of the meteor as a function of its measured radar cross-section. Prior work applies theoretical and computational methods to determine the electron density distribution, but assumes the meteoroid emits neutral particles uniformly across its surface. In this paper, a numerical surface ablation model demonstrates that meteoroid mass loss may occur preferentially in the direction facing the oncoming atmosphere. Specifically, meteoroid mass loss becomes proportional to the frontal surface area facing the freestream atmosphere in the limit of high Biot number, but remains isotropic in the limit of low Biot number. Meteoroid rotation has a small effect on the direction of ejected mass, but the effect is insignificant compared to variation in meteoroid properties that affect the Biot number. This result informs our computational meteor plasma model, in which we compare the effect of meteoroid vaporization on the plasma distribution in the limits of low versus high Biot number. The resulting electron density profiles demonstrate order-of-magnitude agreement between each other, with peak difference of 70% immediately upstream of the meteoroid. This implies that the directional distribution of vaporizing neutrals likely does not significantly influence head echo observations, lending credence to existing work that assumes isotropic ablation.

Plain Language Summary

Meteors entering Earth's atmosphere, colloquially referred to as "shooting stars," are regularly observed by radar instruments that transmit radio waves into the atmosphere and then listen for received signals. Although objects that are meters or larger in diameter pose a collision risk to life on Earth, small particles that are less than millimeters in diameter, called meteoroids, are much more abundant and pose an ongoing threat to spacecraft via high-speed impacts. During entry, a meteoroid collides with oncoming atmospheric particles, causing the meteoroid surface to heat up, melt, and vaporize into gas particles. Previous research assumes this gas is ejected in all directions equally surrounding the meteoroid. We develop a computer simulation that demonstrates that gas may be ejected in greater quantities from the front of the meteoroid facing the oncoming atmosphere. As vaporized gas expands outward, it collides with more atmospheric particles, ionizes, and becomes a plasma. We further perform computer simulations of plasma formation, comparing the cases where meteor material is ejected equally versus preferentially forward. Although the resulting plasma shapes are slightly different between the two cases, the difference is likely not large enough to make a significant difference in radar observations.

1 Introduction

Small extraterrestrial dust particles, known as meteoroids, continuously enter Earth's atmosphere at tens of kilometers per second, colliding with atmospheric species that transfer energy to the meteoroid. As the meteoroid heats, neutral particles vaporize and ionize from its surface, forming a plasma detectable by radar, which is referred to as a meteor. By analyzing meteor radar signatures, properties of the meteoroids responsible for these signatures, in addition to the atmosphere through which they travel, can be better understood and quantified.

Recent research has sought to quantify meteoroid mass and density using their radar or optical signatures (Tarnecki et al., 2021; Tárano et al., 2019; Close et al., 2012). Improving the accuracy of these calculations is important since these properties are directly related to the hazards that such particles pose to spacecraft and astronauts in the space

environment. When meteoroids impact spacecraft, they can cause electrical damage due to generation of a plasma during impact that emits radio-frequency pulses (Kelley et al., 2012; Lau et al., 2024; Lau & Elschot, 2025). The nature of these pulses are known to depend strongly on the properties of the impactor (Garrett & Close, 2013).

As a meteoroid enters Earth's atmosphere and encounters collisions with atmospheric molecules, mass loss occurs from the meteoroid surface due to sputtering and thermal ablation (Popova et al., 2001; Guttormsen et al., 2020). As ablated particles travel away from the meteoroid, they experience further collisions with atmospheric molecules that are often ionizing. A plasma cap forms around the ablating meteoroid, from which radio waves scatter to produce head echo signatures in radar data. As the plasma expands and undergoes more collisions with the surrounding atmosphere, a Farley-Buneman/gradient drift instability may form, initiating turbulence and creating field-aligned irregularities (FAI) (Oppenheim & Dimant, 2015; Oppenheim et al., 2000). When a radar beam is aligned perpendicular to the background magnetic field, these irregularities can Bragg scatter radio waves and create a radar signature known as the nonspecular trail echo (Dyrud et al., 2005). Non-FAI scattering is also known to occur and generate trail echoes in cases where radar beams are not oriented perpendicular to the background magnetic field (Kozlovsky et al., 2020; Chau et al., 2014).

High-power large-aperture (HPLA) radar instruments capable of performing incoherent scatter radar (ISR) measurements are also particularly capable of detecting meteor head echoes. Examples of such radars include the ARPA Long-Range Tracking And Instrumentation Radar (ALTAIR) (Close et al., 2000), the Advanced Modular Incoherent Scatter Radar (AMISR) facilities such as PFISR and RISR-N (Sparks et al., 2010), Millstone Hill Observatory (MHO) (Evans, 1965; Erickson et al., 2001), and Jicamarca Radio Observatory (JRO) (Chau & Woodman, 2004; Y. Li et al., 2020). These facilities observe between hundreds and thousands of meteors per hour (Hedges et al., 2022; Volz & Close, 2012), originating from small particles with diameters of micrometer scale; larger than the particles observed via impact detectors on spacecraft (Baggaley et al., 2007), but smaller than those detectable via optical instruments (Brown et al., 2017; Campbell-Brown & Close, 2007). The abundance of head echo signatures present in radar data can be quickly identified and analyzed using machine learning algorithms (Hedges et al., 2024; Y. Li et al., 2023, 2022). A radar need not be HPLA to observe head echoes; facilities that operate within lower-power regimes such as those adapted from specular meteor radars are also capable of observing head echoes (Janches et al., 2014; Panka et al., 2021).

Previous research has sought to quantify the mass loss rate of a meteoroid using the measured head echo signal strength, along with some model for radio wave scattering from the plasma cap, which can be integrated over the observation time to deduce total meteoroid mass (Marshall et al., 2017). The first such effort is discussed in Close et al. (2004) and Close et al. (2005), in which it is assumed that the electron density surrounding the ablating meteoroid is spherical and drops off in distance via a Gaussian. Bulk density of meteoroids can then be calculated using the measured meteoroid mass and deceleration as input to a model for atmospheric drag (Close et al., 2012). With these properties quantified, one can further apply optimization techniques to calculate atmospheric neutral density as a function of altitude (Limonta et al., 2020; A. Li & Close, 2016). More recent research, including an analytical model based on physical gas dynamics (Dimant & Oppenheim, 2017a, 2017b), demonstrates that the meteor plasma cap shape is far from a Gaussian sphere. This analytical theory, which we henceforth refer to as the DO model, has been validated by a three-dimensional electrostatic particle-in-cell (PIC) simulation (Sugar et al., 2018, 2019). The PIC method is preferable to fluid methods for meteor simulations since it is fully kinetic. Such a method is necessary for meteors since the velocity distributions of ablated particles are expected to be highly non-Maxwellian in the moments after ablation and before they encounter enough equilibrating collisions (Sam et al., 2025). Using a known shape for the plasma surrounding an ablating meteoroid, ra-

dio wave scattering from this plasma can been simulated using the finite-difference time-domain (FDTD) method (Dyrud et al., 2008a, 2008b; Marshall & Close, 2015; Sugar et al., 2021). These analytical and computational approaches rely on the assumption that the meteoroid ablates warm neutrals isotropically, which is generally justified by the argument that the meteoroid is small and rotates quickly.

Given the reliance of prior work on the isotropic ablation assumption, there is an ongoing need to further investigate the directional distribution of ablated neutrals, and understand its effect on the meteor plasma responsible for head echoes. This enables quantification of uncertainty due to this variation in ablation physics, knowledge of which is currently severely lacking in the field. It is known that head echoes sometimes exhibit properties of differential ablation (Dyrud & Janches, 2008; Janches et al., 2009) and fragmentation (Close et al., 2011; Campbell-Brown, 2019), so this work makes a crucial advance towards the most physically accurate ablation simulations that study these effects in detail and quantify their effect on radar observations.

We will first discuss the meteoroid surface ablation model used to demonstrate the importance of considering non-isotropic ablation in section 2. As part of this discussion, we introduce the Biot number for the case where heat transfer occurs primarily due to rarefied collisions between oncoming atmospheric particles and the meteoroid. We then present our computational plasma simulations used to determine the electron density profile of the meteor in section 3, where we consider the extremes of low and high Biot number ablation, and compare the results with an existing analytical theory.

2 Meteoroid Ablation Model

There have been many past works, both analytical and numerical, studying the atmospheric entry of meteoroids, including ablation models (Popova, 2004; Campbell-Brown et al., 2013; Brykina & Egorova, 2023) and flow physics (Zalogin & Kusov, 2016). Effects of rotation have also been studied for simplified cases. Simulations of meteoroid entry for a rapidly rotating meteoroid and a non-rotating meteoroid have been performed to investigate the effects of meteoroid rotation on meteor formation altitude (Adolfsson et al., 1994).

Meteoroids with diameters smaller than 10^{-3} m are often assumed isothermal, such that they eject ablation products during entry with a distribution equiprobable in all directions. The Biot number is often used to justify an isothermal assumption, which is an indicator of the temperature uniformity in a body undergoing heating and is typically defined as $Bi = hL/\lambda$ where h is the convection coefficient, L is a characteristic length scale, and λ is the thermal conductivity of the solid. A small Biot number ($Bi \ll 1$) typically indicates an isothermal condition. In the case of meteoroid entry, since the surrounding flow is not a continuum flow for small meteoroids, the convection coefficient cannot be used and another parameter to represent the heat flux must be considered. Past works (Love & Brownlee, 1991; Longo & Longo, 2018) justify isothermality using a modified Biot number that assumes radiation, rather than convection, is the dominant mode of heat flux from the meteoroid surface, such that $h \approx \sigma T^3$, where σ is the Stefan-Boltzmann constant and T is the characteristic temperature of the ablating meteoroid. This results in the following expression for the Biot number: $Bi = \sigma T^3 L/\lambda$.

This definition of the Biot number results in very small values of Bi for parameters of interest in this study. As a simple model of asteroidal meteoroids, we take $\lambda = 3$ W/(mK) and consider the meteoroid diameter as the characteristic length scale, with $L = 10^{-4}$ m. We show in Section 2.2.1 that the steady-state temperature of this meteoroid traveling at 40 km/s reaches 1750 K. These values yield $Bi = 0.01$, which appears to support the use of an isothermal assumption. In this section, we will investigate whether such a meteoroid is truly isothermal using a surface ablation model, and what this indicates

for the directions in which ablation products are ejected. We also vary meteoroid parameters, including rotation, to determine their effect on ablation.

2.1 Physical Model and Numerical Methods

A simplified 2D model is used to simulate heat transfer within the meteoroid and through its surface. It is assumed that the surface does not recede due to mass loss, to avoid any need to adapt the mesh geometry across each timestep. Energy flux due to vaporization is still considered. The 2D heat equation is solved in cylindrical coordinates:

$$\frac{\partial T(r,\theta)}{\partial t} = \frac{\alpha}{r}\frac{\partial}{\partial r}\left(r\frac{\partial T(r,\theta)}{\partial r}\right) + \frac{\alpha}{r^2}\frac{\partial^2 T(r,\theta)}{\partial \theta^2}, \tag{1}$$

where α is the thermal diffusivity, defined as $\alpha = \lambda/(\rho_m c_p)$ where ρ_m is the mass density of the meteoroid material and c_p is the specific heat capacity of the material. Performing the simulation in 2D effectively approximates the meteoroid as an infinitely long cylinder with the atmosphere impinging on the curved face. Since the fundamental physics of heat transfer are similar in 3D, this model serves as a starting point to assess isothermality and ablation.

The heat flux boundary condition is applied for free-molecular conditions, suitable for high altitude ablation of small meteoroids. Assuming full thermal accommodation, the heat flux from collisions with atmospheric molecules at a given point on the meteoroid surface, in units of power per unit area, is calculated as

$$q_{in} = \frac{1}{2}\rho_a U^3 \cos\beta, \tag{2}$$

where ρ_a is the mass density of the neutral atmosphere, U is the meteoroid speed, and β is the relative angle between a surface element normal vector and the meteoroid velocity vector. For elements on the back side of the meteoroid, the heat flux is set to zero.

Heat rejection from radiation and vaporization at the surface is also considered, yielding the net heat flux through a surface element as:

$$q_{net} = \frac{1}{2}\rho_a U^3 \cos\beta - \sigma\epsilon T_s^4 - H\Big(\frac{1}{s}\frac{dm}{dt}\Big), \tag{3}$$

where ϵ is the emissivity, T_s is the surface temperature, H is the latent heat of vaporization, and $\frac{1}{s}\frac{dm}{dt}$ is the mass loss per unit area from the surface where s is the area of the surface element.

Following the simplified ablation models in the literature (Popova, 2004; Zalogin & Kusov, 2016; Adolfsson et al., 1996), we compute

$$\frac{1}{s}\frac{dm}{dt} = P_v\Big(\frac{\mu}{2\pi k_b T}\Big)^{1/2}, \tag{4}$$

where μ is the molecular mass, k_b is the Boltzmann constant, and P_v is the vapor pressure, calculated with the Clausius-Clapeyron model:

$$\log_{10} P_v(T) = C_A - \frac{C_B}{T}, \tag{5}$$

where C_A and C_B are the Clausius-Clapeyron coefficients. A slightly modified form of this model was used by Zalogin and Kusov for the study of iron meteoroid entry (Zalogin & Kusov, 2016).

The equations are solved with a 2nd order finite differencing scheme for the spatial derivatives and implicit Euler for the time derivative. The Scipy library (Virtanen et al., 2020) is used for the sparse matrix construction and solving the linear system of

the meteoroid can be assumed relatively constant. With the parameters defined in Table 1, the diffusion timescale specified by R^2/α is 2.5 ms. Using the time it takes for a 40 km/s meteoroid to travel 1 km gives a time interval of 25 ms. The Fourier number is 10 in this case, which indicates that a steady-state analysis of the meteor temperature profile is appropriate.

An initial simulation was performed of this asteroidal meteoroid without rotation, the results of which are shown in Figure 1. We can see that, starting from an initial temperature of 300 K, a steady-state solution with average temperature $\bar{T} \approx 1750$ K is reached at around 0.03 s, with a difference between temperature extremes of 138 K. Although the meteoroid appears reasonably isothermal, the ablation rate is highly non-uniform across the surface. This is because relatively small differences in the temperature can result in significant differences in the ablation rate, which is specified by its nonlinear relationship with temperature in Equations 4 and 5. We calculate the overall probability density function of the direction that a particle is ejected, θ, by assuming that all particles are ejected from any given surface point with probability given by a half-Maxwellian distribution and then integrating the directional distribution of mass loss per unit area across the surface. In summary, these results indicate that for a non-rotating meteoroid, temperature differences on the order of 100 K may exist, despite the modified Biot number (with $h \approx \sigma T^3$) predicting isothermal behavior. Such a temperature difference leads to a surface ablation rate multiple times larger in the upstream-facing direction than the downstream-facing direction.

2.2.2 Effects of Rotation

Next, we consider the effects of rotation on the isothermal assumption, particularly as it relates to the distribution of ejected ablation products. Some past works have attempted to estimate the rotation of meteoroids. Beech and Brown used flickering in optical meteoroid observational data as an indirect measurement of rotation rate (Beech & Brown, 2000), with frequencies up to 500 Hz observed for meteoroids as small as 1 cm in diameter. Capek performed numerical estimations of the rotation rates of cometary meteoroids, estimating a median rotation frequency of around 100 Hz for 1 mm diameter meteoroids (Čapek, 2014). The results were dependent on the meteoroid diameter, with smaller meteoroids having a higher rotation frequency.

Based on these estimates of meteoroid rotation, we perform simulations with 100 Hz, 500 Hz, and 1000 Hz rotation with the same conditions detailed in Table 1. The resulting steady-state temperature profiles are shown in Figure 2b, including the prior result with no rotation. The rotation produces three main effects on the temperature field: first, the solution becomes more homogeneous for higher rotation rates; second, the average temperature of the meteoroid increases slightly with increasing rotation rates; and finally, the location of maximum temperature is shifted in the direction of rotation, with the magnitude of the shift increasing with the rotation rate. The magnitude of these effects are shown in Table 2. In each case, a steady state is reached and the time to reach steady-state from an initial temperature of 300 K is not significantly affected by the rotation rate.

As expected, these results impact the steady-state distribution of the ejected ablation particles, which are shown in Figure 2a. As the rotation frequency increases, the distribution of ejected particles becomes more uniform, and the peak of the distribution shifts away from the direction of the incoming free-stream in the direction of the rotation. This shift corresponds exactly to the shift in maximum temperature. Importantly, even at 1000 Hz rotation, there is significant variability in the distribution of ejected particles, with a ratio of maximum to minimum ablation rates of 1.58 at 1000 Hz (as a comparison, the ratio is 2.98 at 0 Hz).

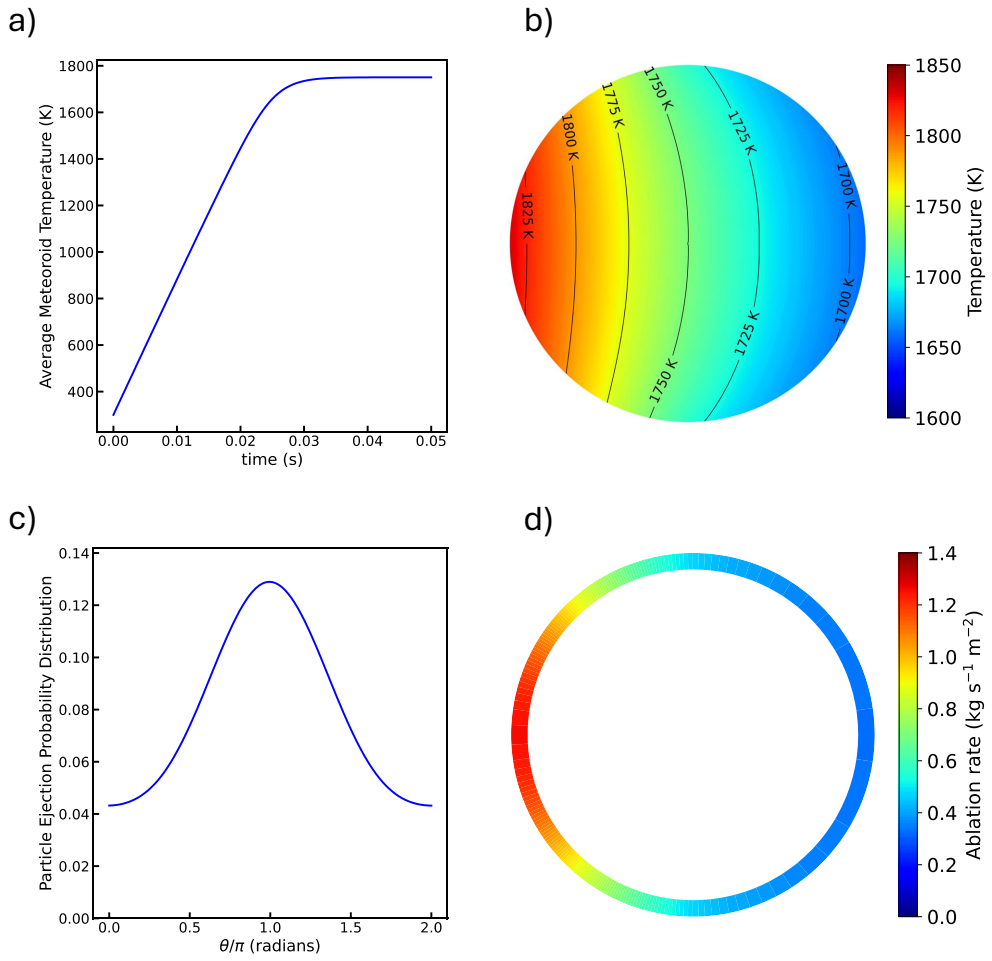

Figure 1. Surface ablation model results for an asteroidal meteoroid with diameter of 10^{-4} m ablating at 100 km showing a) the average temperature of the meteoroid as a function of time, b) the steady-state temperature profile of the meteoroid, c) the probability density function of the ejected direction of particles from the meteoroid, and d) the ablation rate as a function of position on the meteoroid surface. Temperature fields are visualized with the atmosphere traveling from left to right.

Table 2. Results from surface ablation simulations for the variation in temperature as a result of varying rotation rate.

Rotation Rate	Mean Temp. (K)	Temp. Range (K)	Temp. Peak Shift (Radians)
0 Hz	1750.2	137.6	0
100 Hz	1751.1	133.5	0.142
500 Hz	1757.3	90.90	0.481
1000 Hz	1759.3	64.07	0.550

Although increasing the meteoroid rotation rate does make the solution more isothermal, given the nonlinear relationship between the temperature and the ablation rate, it is clear that rapidly rotating meteoroids can still have relevant temperature gradients

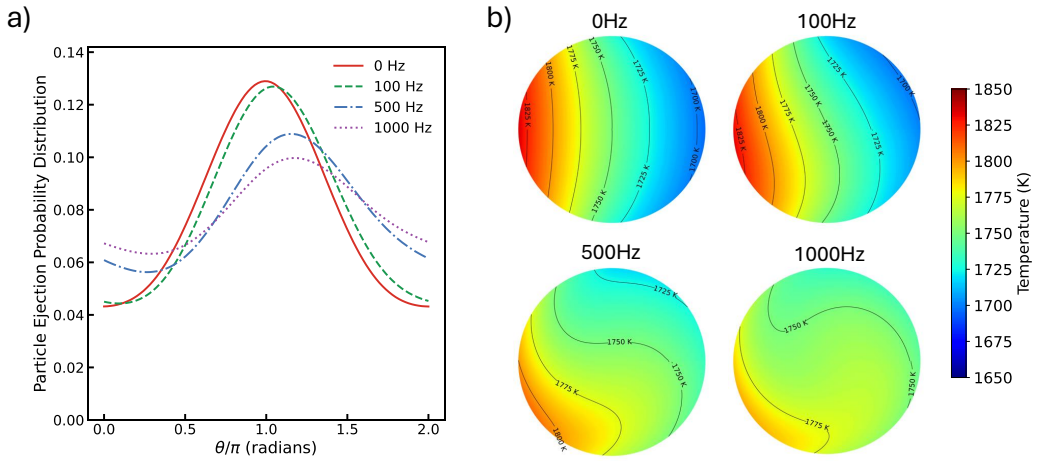

Figure 2. Surface ablation model results for an asteroidal meteoroid of $d = 10^{-4}$ m at 100 km for 0 Hz, 100 Hz, 500 Hz, and 1000 Hz rotation rates showing a) the probability density function of the ejected direction of particles from the meteoroid and b) the steady-state temperature profile of the meteoroid.

resulting in significant variation in ejected particle distribution. Furthermore, this variation can occur in spite of very low Biot numbers as defined using the $h \approx \sigma T^3$ convention used previously in the literature.

2.2.3 Revisiting the Biot number

Our result of significant temperature gradients at a low Biot number motivated further investigation of the Biot number definition used in past works (Love & Brownlee, 1991; Longo & Longo, 2018). One potential problem with this definition lies in the substitution of the convection term given by $h \approx \sigma T^3$, which implicitly assumes that radiation is the dominant mode of heat transfer in the problem. Revisiting the equilibrium energy balance specified by Equation 6, the heat flux from the free-molecular flow collisions is balanced against the endothermic vaporization reaction and the radiative heat transfer from the meteoroid. For our simulation parameters in Table 1, the radiation accounts for roughly 12.4% of this balance, with the remaining 87.6% of the heat losses attributed to vaporization. A more appropriate definition of the Biot number may therefore be one that captures the heat flux experienced by the meteoroid more directly. Here, we instead define the Biot number based on the heat flux per unit area experienced by the meteoroid under rarefied flow conditions, with $h \approx \rho_a U^3 / T$ and

$$Bi = \frac{\rho_a U^3 L}{T \lambda}. \tag{8}$$

Applying this definition of the Biot number to the conditions of our aforementioned simulations yields $Bi = 0.53$, as compared to a value of $Bi = 0.01$ with the previous definition. While the current formulation is defined for free-molecular flow conditions, it could be extended to account for transitional and continuum flow conditions.

To study the effect of our Biot number definition on the final solution, the thermal conductivity of the meteoroid was modified to yield Biot numbers of 10, 1, 0.1, and 0.01. It should be noted that modifying the meteoroid radius to yield the same Biot numbers produces the same steady state solution. Other material and entry properties were

unchanged. Simulations were then performed for 0 Hz, 100 Hz, and 1000 Hz rotation rates. Results are presented in Figure 3, and the modified Biot number is shown to provide a reasonable measure of the homogeneity of the ejected particle distributions. For higher Biot numbers ($Bi \gtrsim 1$), the solution shows significant variation, and for low Biot numbers ($Bi \ll 1$), an isothermal assumption holds. Notably, when $Bi = 10$, the ejection probability trends toward a sinusoidal function, where particles are most likely to be ejected upstream (i.e. in the direction of the meteoroid velocity vector). This indicates that particles at any given point on the meteoroid surface are ablated at a rate proportional to the surface area that faces the oncoming atmosphere. As expected, the rotation rate impacts the solution homogeneity, but the same trend with the Biot number is still observed. In additional simulations, it was found that varying the Biot number by changing either the diameter or the thermal conductivity produced identical final results in the temperature field and ablation product ejection distributions.

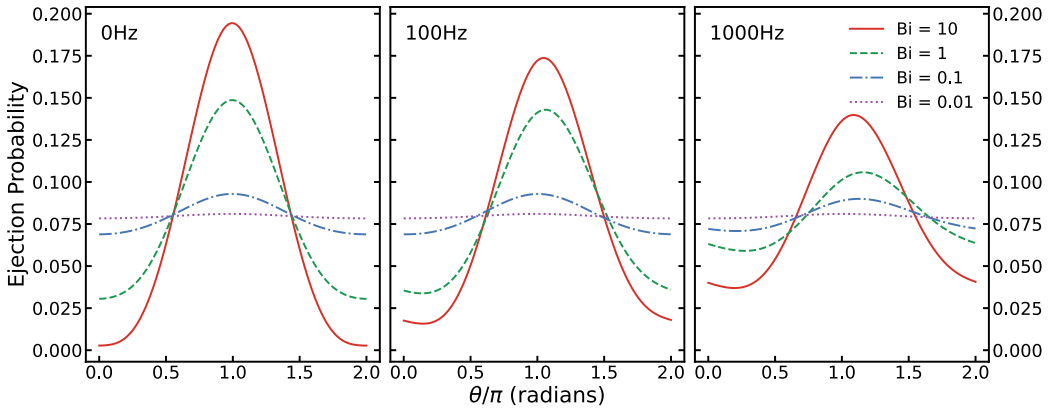

Figure 3. Ejection direction probability distribution functions for Biot numbers of 10, 1, 0.1, and 0.01 at rotation rates of 0 Hz, 100 Hz, and 1000 Hz. These results correspond to simulations where the Biot number is controlled by modifying the thermal conductivity. Identical results are produced by modifying diameter.

Figure 4 depicts the same simulation setup per the parameters specified in Table 1, except the atmospheric altitude (and therefore density) is now varied to yield Biot numbers of 10, 1, 0.1, and 0.01. We further recompute the characteristic temperature by solving the energy balance in equation 6. This is necessary when either the density or velocity is modified. While the results in Figures 3 and 4 are not identical, the qualitative trend captured in our Biot number definition, specified by Equation 8, holds regardless of which parameters are modified. The main difference between these results is the impact of the rotation on the overall solution. Since the high density (and therefore high heat flux) solutions in Figure 4 heat the meteoroid very quickly, the impact of the rotation is reduced.

2.2.4 Key Takeaway

In summary, a small numerical study was conducted on meteoroid heating, rotation, and ablation using a simplified 2D model. The key takeaway from this study is that significant temperature gradients can exist under conditions often considered to be isothermal. Under such conditions, these temperature gradients result in a non-uniform distribution of ejected ablation products from the meteoroid. The commonly used definition for the Biot number (where $h \approx \sigma T^3$) does not appropriately predict these inhomogeneities. Instead, a modified Biot number is proposed and simulations are presented for a range

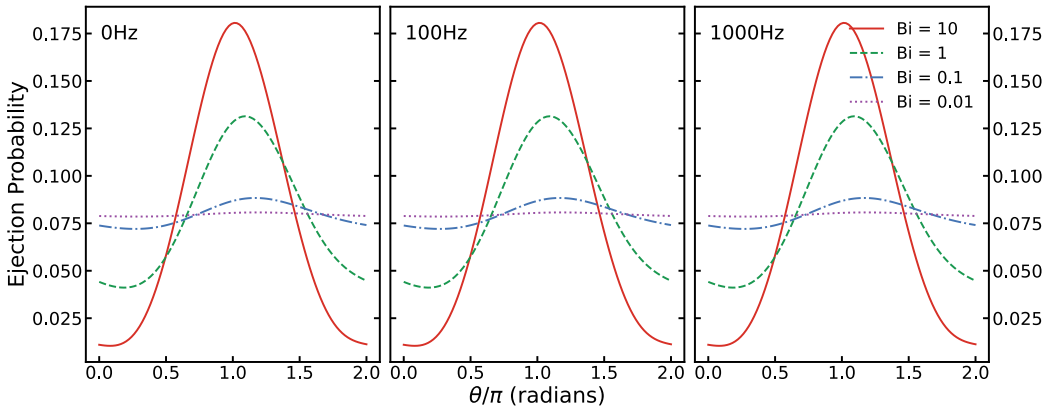

Figure 4. Ejection direction probability distribution functions for Biot numbers of 10, 1, 0.1, and 0.01 at rotation rates of 0 Hz, 100 Hz, and 1000 Hz. These results correspond to simulations where the Biot number is controlled by modifying the atmospheric density. Identical results are produced by modifying entry velocity to achieve the same changes in the free-molecular heat flux.

of modified Biot numbers and rotation rates. When $Bi \gg 1$, the ejected particle distribution is highly heterogeneous, and suggests that a given point on the meteoroid surface ablates at a rate approximately proportional to the surface area facing toward the oncoming atmosphere. When $Bi \ll 1$, the ejected particle distribution is nearly isotropic, as per the assumptions of many prior models for meteoroid ablation. Rotation can increase the isotropy of ablation to some extent, but the effect is not nearly as pronounced as that of changing the Biot number.

Although this ablation simulation was performed in two dimensions, which effectively approximates the meteoroid as an infinitely long cylinder rather than a sphere, the result provides a starting point to investigate how non-isotropic ablation may influence plasma formation and radar observations of the meteor head echo. Although a three-dimensional ablation simulation would be more physically accurate, determining how the meteoroid tumbles in 3D is not trivial, and since the physics of heat and mass transfer are similar, we do not expect these key findings to vary drastically in 3D. We further investigate the effect of varied Biot number on plasma formation using a 3D plasma simulation in Section 3.

3 Plasma Simulation

Since the plasma surrounding an ablating meteoroid is responsible for the head echo signature, we seek to simulate this plasma as accurately as possible to best interpret the plethora of head echoes present in radar data. As part of this effort, we incorporate the physical understanding gained via our ablation model into our models of the plasma that is directly observed by radar instruments.

Prior efforts to simulate plasma in the near-meteoroid region make significant assumptions in how ions and electrons from the ablating meteor are initialized within the simulation domain. The first such investigation by Jones et al. (1999) tracks the motion of ablated particles and the momentum-scattering and ionization effects that occur due to collisions with background neutral particles. However, thermally ablated neutral atoms are initialized at zero velocity, which neglects the initial motion of ablating particles before they collide with atmospheric particles. Furthermore, it is not a full PIC simulation since the effect of the electric field acting on ions and electrons is neglected. The second

attempt to perform meteor head echo simulation by Dyrud et al. (2008a) utilized a two-dimensional PIC code to resolve the meteor plasma including the effects of the electric field, but this simulation effectively assumed that ions are directly ablated from a point source via sputtering, rather than assuming neutrals are thermally ablated at some finite velocity before ionizing some distance away from the meteoroid due to a collision.

The most recent PIC simulation of the meteor head echo by Sugar et al. (2019) used the massively parallel three-dimensional Electrostatic Parallel Particle-in-Cell (EPPIC) code on a supercomputer (Oppenheim et al., 2008), which tracks meteoric neutrals, ions, and electrons along with background ionospheric ions and electrons, while modelling background atmospheric neutrals as a continuum. The simulation assumes warm neutrals are initialized isothermally, with equal probability that a neutral particle is ejected from any part of the meteoroid. Ionization occurs subsequently after the neutral particle travels some distance from the meteoroid and collides with an atmospheric neutral particle.

Despite Sugar et al. (2019) being the most accurate meteor head echo plasma simulation to date, the ablation model results discussed in Section 2 demonstrate that warm neutrals are not ejected isotropically from many of the meteoroids that generate head echoes observed via radar, which raises the question of how this effect influences the electron density shape surrounding the meteoroid, and therefore how radio waves reflect from the plasma. In the following section, we will discuss the implementation of a non-isotropic ablation case into EPPIC based on the ablation model results, and then compare the difference between the plasma shape calculated via this non-isotropic case and the formerly used isotropic ablation case. We further compare the results from both cases with the analytical DO model developed by Dimant and Oppenheim (2017a, 2017b).

3.1 Simulation Method

We performed our PIC simulations using the EPPIC code running on a supercomputer cluster. EPPIC is an electrostatic PIC code that performs computation in three dimensions on a uniform Cartesian grid.

For our meteor plasma simulations, we track five particle species: meteoric neutrals, meteoric ions, meteoric electrons, ionospheric ions, and ionospheric electrons. We take the meteoric neutral particles to be purely sodium particles, since spectral observations reveal that sodium is quite common in meteor observations (Ceplecha et al., 1998). Although simulations including varying or multiple elements would be interesting, it is not the focus of this study. Ionospheric ions and electrons are initialized uniformly throughout the domain with a Maxwellian velocity distribution at a given temperature.

Atmospheric neutrals are treated as a uniform fluid of nitrogen gas particles travelling at constant velocity relative to the meteoroid, since they are far more numerous relative to the other species and therefore including them as discrete particles would be computationally prohibitive. On each timestep, the present particle positions are used to calculate species densities, and thus total charge density, ρ, everywhere on the grid. The electrostatic potential, ϕ, is then calculated using Poisson's equation derived via Gauss' Law,

$$\nabla^2 \phi = -\frac{\rho}{\epsilon_0}, \tag{9}$$

where ϵ_0 is the vacuum permittivity. Poisson's equation is discretized and solved on the 3D simulation grid by leveraging fast Fourier transforms in the dimensions perpendicular to the meteoroid trajectory, and then solving the equation directly via a tridiagonal matrix solution in the remaining dimension. The use of Fourier methods accelerate computations in directions where it is acceptable to assume the boundary conditions are periodic.

The electric field is computed via the definition of electrostatic potential, $\vec{E} = -\nabla\phi$, at the position of each particle, from which the particle's velocity at the next timestep is determined via

$$\Delta\vec{v} = \frac{q}{m}\left(\vec{E} + \vec{v} \times \vec{B}_0\right)\Delta t, \tag{10}$$

where q and m are the particle's charge and mass, respectively, $\vec{B}_0$ is the background geomagnetic field vector, and Δt is the timestep length. Given the electrostatic solution, we assume that the magnetic field induced by the plasma itself is not strong enough to significantly alter the results. Once the new particle velocity is calculated, the effect of momentum-scattering collisions with atmospheric neutral particles is accounted for using the Monte Carlo Collision (MCC) method (Birdsall, 1991), which updates the velocity vectors of some neutrals, ions, and electrons. Particle positions are then simply updated via the relation $\Delta\vec{r} = \vec{v}\Delta t$.

3.1.1 Simulation Parameters

For a small meteoroid entering Earth's atmosphere at an altitude of 100 km and velocity of 40 km/s, Sugar et al. (2019) determined that the simulations require a domain size of 2.56 m in all three dimensions to ensure the meteor head plasma is fully captured, and a cell length of $5{\times}10^{-3}$ m in all three dimensions to ensure the plasma Debye length is resolved throughout the domain, including at the position of peak plasma density. The computational grid therefore includes 512 points per dimension. Ideally, we would resolve the length scale of the meteoroid surface within our PIC plasma simulation and include surface physics such as charging, but it is currently computationally prohibitive to use a grid resolution small enough when the meteoroid diameter is set to 0.1 mm.

We use a simulated electron mass of 10 times the physical electron mass in order to increase the allowable timestep size. This technique is frequently used in PIC simulations to decrease the computational time necessary to run the simulations while preserving accuracy (Bret & Dieckmann, 2010). A timestep size of 20 ns then ensures that plasma oscillations are resolved throughout the domain. We consider background ions to have the same mass as meteoric ions since the mass of sodium is very similar to the mass of nitrogen gas and therefore does not significantly affect the results.

In our simulation, at time $t = 0$, we initialize the domain with a background ionospheric plasma of uniform density throughout the domain, and we begin to initialize ablated neutral particles at the meteoroid location. After enough timesteps have been computed, the number of total particles in the simulation reaches a quasi-steady value. At this point, the simulation has reached a steady state, and we consider the results for quantities such as density and electrostatic potential final.

Since our meteor simulations evolve into a steady state within a timescale of microseconds, and meteor entry typically occurs on a larger timescale of tens to hundreds of milliseconds, we choose background conditions that are constant and consistent with our chosen altitude of 100 km. We set the background neutral atmospheric number density to 1.1×10^{19} m^{-3}, and the background ionospheric species number densities to 1.9×10^{9} m^{-3} with a temperature of 380 K, corresponding to a quiet nighttime ionosphere. We initialize meteoric particles such that one simulated particle represents 2048 physical particles, and initialize background ionospheric particles such that one simulated particle represents 256 physical particles. We orient the background magnetic field perpendicular to the meteor trajectory. As an example, this condition would be expected for a meteor descending from directly overhead at Jicamarca Radio Observatory. We assume the meteoroid ablates at a total rate of $\dot{m} = 10^{-11}$ kg/s. This value is lower than what we expect for many head echoes observed in HPLA radar data, but increasing it further would reduce the smallest Debye length and therefore require reducing the simulation cell size. We tested varying the simulated value of $\dot{m}$, and doing so results in directly proportion-

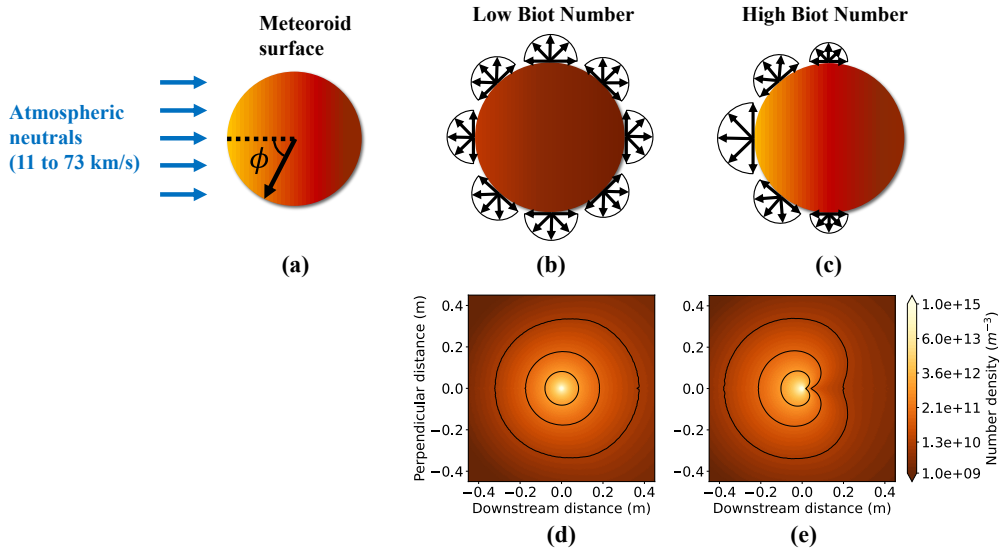

Figure 5. Illustration of how thermally ablated neutral particles are initialized in the simulation, including a) definition of angle ϕ, diagrams of particle initialization for b) low Biot number and c) high Biot number, and simulated neutral particle density in steady-state within the domain for d) low Biot number and e) high Biot number. The diagrams showing the meteoroid surface are for illustration only; in the plasma simulation, this surface reduces to a point source.

ate scaling of the plasma density. The results also remain in agreement with the DO model. Thus, although the simulated plasma density will be overall lower than what occurs in many real meteors, we can assume that the plasma shape is representative of the shape that appears at higher ablation rates, up to the point where collisions between two meteoric particles, as opposed to collisions involving one meteoric particle and one atmospheric particle, become frequent enough to alter the plasma shape.

3.1.2 Meteoric Particle Initialization

Since the grid spacing is 50 times larger than the diameter of the meteoroid examined via our computational ablation model, we consider the meteoroid a point source of warm neutral particles at 2500 K, where each neutral is generated given the probability that its initial velocity has a particular magnitude and direction.

We initialize warm neutral particles via a two-step process. The first step is to choose a point on the meteoroid surface corresponding to the point at which the particle vaporizes, using some probabilistic model specifying the odds a particle is ablated from any given point on the surface. The second step is to assign a magnitude and direction to the velocity vector of the particle, assuming the probability it is ejected in any given direction is specified via a half-Maxwellian oriented normal to the meteoroid surface at the point chosen via the first step. This process is illustrated in Figure 5. Note that since the meteoroid surface is so small relative to the grid, the particle position on the surface is not modelled, and this position is only relevant for determining the direction of the half-Maxwellian distribution from which it is initialized.

In the material ablation simulations with high Biot number, it is observed that the ejection probability trends toward a value that is proportional to the projected surface area facing upstream at any given point, with far reduced ablation occurring from the side facing downstream. The ablation rate per unit area at any point on the surface is

thus $\dot{m}' \sim \cos(\phi)$, where ϕ is the angle between a given surface point and the point on the meteoroid directly facing upstream (i.e. aligned with the meteoroid velocity vector), and $\int_A \dot{m}' dA = \dot{m}$. Straightforwardly, in simulations with low Biot number, the ejection probability is constant across angle. We therefore simulate the two extremes of high and low Biot number in separate PIC simulations, to determine how varying Biot number may affect the meteor plasma, and thus influence radar head echo observations.

3.1.3 Collisions and Ionization

Since the background atmospheric neutral density is multiple orders of magnitude higher than the densities of each meteoric species, we include only collisions between each meteoric species and background atmospheric neutral particles in our PIC simulation. Via the MCC method, the chance that particle collides with an atmospheric neutral within the length of a timestep is given by

$$P_m = 1 - \exp(-n_A \sigma V_{rel} \Delta t), \tag{11}$$

where n_A is the background atmospheric density, σ is the collisional cross section, and V_{rel} is the magnitude of the relative velocity between the colliding particles. We assume that collisions between meteoric neutrals and atmospheric neutrals have the same cross-section as between meteoric ions and atmospheric neutrals, since Sugar et al. (2018) demonstrates that the difference is less than 1% via analysis of Lennard-Jones interaction potential models. We then determine this cross-section using an empirical formula that has been used frequently in prior research (Bronshten, 1983). Therefore,

$$\sigma_{nn} = \sigma_{in} = 5.61 \times 10^{-19} V_{rel}^{-0.8}, \tag{12}$$

where V_{rel} must be specified in kilometers per second. These collisions are considered to be fully elastic, since the ionization energy of sodium is significantly less than the total collision energy at velocities in the range expected for meteors. For collisions between electrons and atmospheric neutrals, we instead assume that inelastic collisions dominate, since Figure 7 of Frost and Phelps (1962) demonstrates that inelastic collision rates at energies around 1 eV and below are multiple orders of magnitude larger than elastic collision rates. We then model inelastic energy loss via the method discussed in Oppenheim et al. (2008) and Oppenheim and Dimant (2013). The collisional cross-section for electron-neutral collisions at velocities below 400 km/s is determined by the formula specified in Gurevich (1978),

$$\sigma_{en} = \left(1.6246 \times 10^{-23}\right) V_{rel}^{\frac{2}{3}}, \tag{13}$$

where V_{rel} must be specified in meters per second. For velocities above 400 km/s, the cross sections are interpolated from Figure 1 in Engelhardt et al. (1964).

In the event that a neutral particle undergoes momentum scattering, its probability of ionization is assessed using the empirical power law specified by Vondrak et al. (2008) for sodium particles,

$$\beta = 0.933 \left(V_{rel} - 8.86\right)^2 V_{rel}^{-1.94}, \tag{14}$$

where V_{rel} must be specified in kilometers per second. If ionization occurs, the neutral particle is replaced with an ion and an electron. The ion undergoes momentum scattering via the MCC method, while the electron is initialized with random direction and with its velocity magnitude sampled from a 1 eV Maxwellian distribution relative to the collision center of mass. This method of initializing electrons is based on the work of Berry (1961) and is further discussed in Sugar et al. (2019). Since spectroscopic observations demonstrate that most ions are singly ionized species, we do not include any multiply ionized species in our simulation (Ceplecha et al., 1998).

3.1.4 Boundary Conditions

In order to reduce overall computation time and leverage the performance improvement gained by the use of fast Fourier transform methods, we use periodic boundaries in both dimensions perpendicular to the direction the meteor travels. Although this effectively simulates a two-dimensional array of meteors in parallel, so long as there is no significant population of meteoric particles crossing the periodic boundaries, the assumption does not significantly impact results. Particles that exit a periodic boundary will re-enter from the opposite side, and electrostatic potential is inherently assumed periodic at the corresponding boundaries when calculated via the Fourier method.

We cannot use a third periodic boundary in the direction of the meteor trajectory, since the outgoing meteor trail would nonphysically overlap with the meteor head echo plasma. These boundaries act as inflow and outflow boundaries for the neutral atmosphere and background ionosphere. Since only the background ionosphere needs to be resolved via particles, we inject ionospheric ions and electrons at each of the boundaries using a Maxwellian flux distribution with the bulk velocity of the relative atmospheric motion. The results of Sugar et al. (2019) demonstrate that Neumann field boundary conditions at the nonperiodic boundaries, where $\nabla\phi = \vec{E} = 0$, are appropriate for meteor plasma simulations with a quiet ionosphere, so we employ this condition for the field potential.

3.2 Simulation Results

Since the magnetic field only contributes to minor asymmetry in the results, and studying its effect is not the primary motivation of this paper, we present the electron density profiles axially averaged about the meteor trajectory. Furthermore, to mitigate the noise that is inevitable in PIC simulation results, we perform time-averaging of the steady-state result by outputting the electron density field every 25 simulated timesteps, until the results from 400 timesteps are output. These fields are averaged together.

The electron density for the cases of low-Biot and high-Biot meteoroids, along with the electron density predicted by the DO model, the percent difference between the low-Biot and high-Biot cases, and the percent difference between each simulation and the DO model, are compared in Figure 6. From visual inspection of the logarithmic contour plots, the electron density shapes are remarkably similar between the low-Biot and high-Biot cases, and even the DO model in the near-meteoroid head echo region. The percent difference plot between the low- and high-Biot cases reveals the difference between the shapes. In the region directly upstream of the meteoroid, there is greater than 60% difference, and in the region directly downstream, the difference is up to 40%. This is intuitive given that the difference in neutral ablation is greatest in front of and behind the meteoroid, and differences in the neutral densities drive differences in the electron densities as neutrals quickly ionize after vaporizing.

It is clear that the DO model produces the greatest similarity in the near-meteoroid region, as expected given that the DO model is intended specifically to resolve this region. The DO model neglects a component of forward scattering of ionized particles, which explains the apparent discontinuity between the upstream and downstream components of the plasma, and the reduced upstream agreement between the DO model and PIC plasma densities. For the low-Biot case, agreement is very strong downstream of the meteoroid, with less than 50% difference until beyond 0.5 meters downstream. For the high-Biot case, agreement in this region is not as strong, with up to 100% difference close to the meteoroid. This makes sense given that the DO model effectively assumes a low Biot number via isotropic ablation. In both cases, the percent difference increases with distance from the meteoroid. The percent difference blows up in the upstream direction beyond the region occupied by the meteor plasma. This is because the DO model neglects the

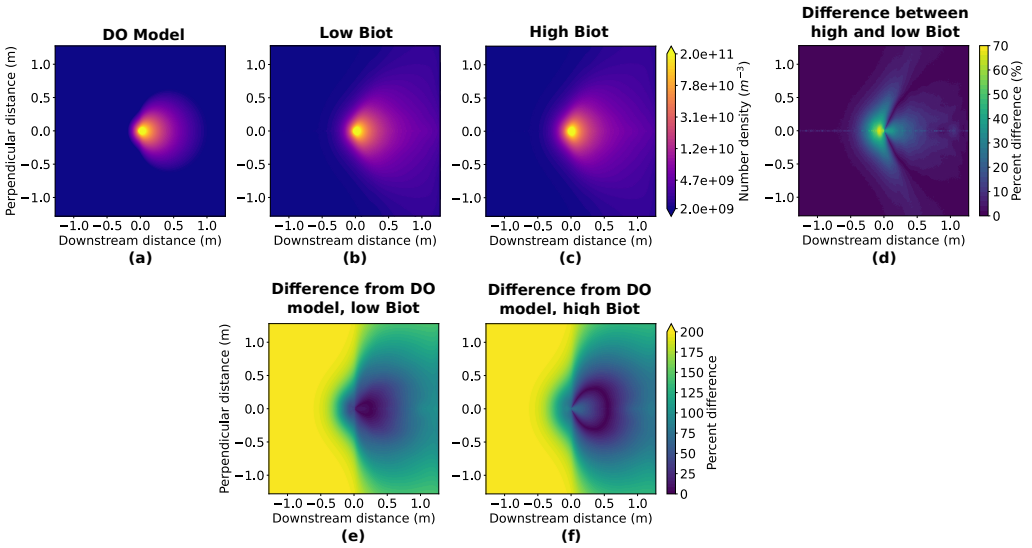

Figure 6. Electron density for a) the DO model, electron density for b) the low-Biot and c) high-Biot PIC cases averaged about the axis of the meteor trajectory, d) difference between the two PIC cases, and e) and f) difference between each PIC case and the DO model.

background ionosphere included within the PIC simulations and the density drops to zero in this region.

To more clearly elucidate how the electron density varies between the low- and high-Biot cases, we consider the axially averaged electron densities along lines perpendicular to the meteor trajectory, depicted in Figure 7. Slightly upstream of the meteoroid position, the plasma density is larger overall for the high-Biot case, due to greater ejection of neutral particles from the side of the surface facing upstream. Progressing downstream, the high-Biot plasma density is lower in the near-meteoroid region but then becomes larger at greater perpendicular distance.

In general, the plasma density shapes agree within an order of magnitude between the extreme low-Biot and high-Biot cases. In reality, for many meteors, it is likely that the plasma density will fall somewhere in the middle of the two extremes, given the variation in rotation, size, material, and atmospheric properties. The shape variation may contribute somewhat to differences in the observed radar signal strength, although the effect is not likely to be drastic. Furthermore, the simulation results lend additional credence to the analytical DO model, given that variation within the near-meteoroid plasma region is minor, and this region is responsible for generating head echoes in radar data. For non-fragmenting and near-spherical meteoroids, where the ablation rate is not large enough for a vapor cap to form, the DO model is a sufficient physical picture of the plasma responsible for head echo scattering.

4 Conclusions and Future Work

In this paper, a numerical model for ablation and surface recession of meteoroids with varying properties including rotation rate is developed. Although prior work defines a meteoroid Biot number based on radiative heat transfer, we suggest a Biot number based on atmospheric heating; we show that this modified Biot number better predicts the thermal gradients present during meteoroid entry. Our meteoroid heat transfer and ablation model demonstrates that meteoroids with moderate to large Biot num-

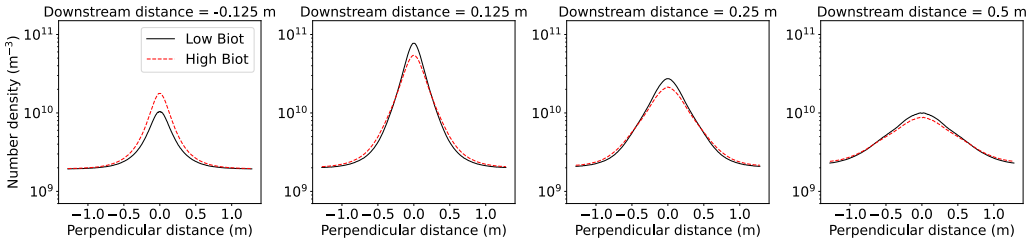

Figure 7. Axially averaged electron density profiles from each PIC case along a line perpendicular to the trajectory axis at varying downstream distances.

ber, even at high rotation rates, do not experience isotropic ablation. This result is contrary to what has extensively been assumed for prior meteoroid ablation research. Instead, ablation becomes proportional to the projected surface area facing upstream. The results motivate the extension of our existing PIC plasma simulation of an ablating meteor to account for anisotropic ejection of ablating neutrals. Using our PIC code, we simulate the extremes of low-Biot and high-Biot number ablation. Although the electron density shape varies somewhat between the cases of isotropic and non-isotropic ablation, the difference overall does not exceed 70%, and the shapes are very similar within order-of-magnitude scale.

It must be noted that this work purely investigates the potential effect of anisotropic ablation that may be dependent on rotation, among other parameters, for the case of a spherical non-fragmenting meteoroid. Our simulations are an important step towards advanced models of radio wave scattering that may explain more unique head echo observations in HPLA radar data. Future work will investigate surface recession in the very likely case that an incoming meteoroid is more irregularly shaped and composed of varying material, and move towards self-consistent three-dimensional simulation of surface recession and tumbling. This will more accurately quantify the range of rotation rates expected for incoming meteoroids, and further investigate how the plasma density profile that generates a head echo may vary based on meteoroid properties. Additionally, computational simulation of radio wave scattering using the FDTD method will be carried out using PIC results for the electron density shape. This will specify how much the radar cross-section of a measured head echo might vary due to variation in the ablation parameters of a meteoroid.

Data and Code Availability Statement

All of the code repositories and data necessary to reproduce the results of this paper are archived on the Stanford Digital Repository at `https://doi.org/10.25740/hm841hz7021` (Hedges et al., 2025). For chapter 2, this includes the code used to run the surface ablation model, generate results, and recreate each figure. For chapter 3, this includes the version of the EPPIC code used to perform the electrostatic PIC simulations, the input files for EPPIC, data files containing key results output by EPPIC for each simulation case, and code that uses the results to generate each figure.

Acknowledgments

This work was supported by NSF Grants AGS-1920383, AGS-2048349, and AGS-2301645. High-performance computing resources for PIC simulations were provided via the Texas Advanced Computing Center through ACCESS allocations TG-ATM23011 and TG-ATM100026,

supported by NSF grants #2138259, #2138286, #2138307, #2137603, and #2138296 (Boerner et al., 2023).

References

Adolfsson, L. G., Gustafson, B. Å., & Murray, C. D. (1994). Effect of meteoroid rotation on atmospheric entry heating and meteor beginning height. *Planetary and Space Science*, *42*(8), 593–598.

Adolfsson, L. G., Gustafson, B. Å., & Murray, C. D. (1996). The martian atmosphere as a meteoroid detector. *Icarus*, *119*(1), 144–152.

Baggaley, W. J., Marsh, S. H., & Close, S. (2007). Interstellar meteors. *Dust in Planetary Systems*, *643*, 27–32.

Beech, M., & Brown, P. (2000). Fireball flickering: The case for indirect measurement of meteoroid rotation rates. *Planetary and Space Science*, *48*(10), 925–932.

Berry, H. W. (1961). Energy distribution of electrons from ionizing collisions of heavy particles. *Phys. Rev.*, *121*, 1714–1719. doi: https://doi.org/10.1103/PhysRev.121.1714

Birdsall, C. (1991). Particle-in-cell charged-particle simulations, plus Monte Carlo collisions with neutral atoms, PIC-MCC. *IEEE Transactions on Plasma Science*, *19*(2), 65-85. doi: https://doi.org/10.1109/27.106800

Boerner, T. J., Deems, S., Furlani, T. R., Knuth, S. L., & Towns, J. (2023). ACCESS: advancing innovation: NSF's advanced cyberinfrastructure coordination ecosystem: services & support. In *Practice and experience in advanced research computing 2023: Computing for the common good* (p. 173–176). New York, NY, USA: Association for Computing Machinery. doi: https://doi.org/10.1145/3569951.3597559

Bret, A., & Dieckmann, M. E. (2010). How large can the electron to proton mass ratio be in particle-in-cell simulations of unstable systems? *Physics of Plasmas*, *17*(3), 032109. doi: https://doi.org/10.1063/1.3357336

Bronshten, V. A. (1983). *Physics of meteoric phenomena*. Dordrecht/Boston/Lancaster: D. Reidel Publishing Company. doi: https://doi.org/10.1007/978-94-009-7222-3

Brown, P., Stober, G., Schult, C., Krzeminski, Z., Cooke, W., & Chau, J. L. (2017). Simultaneous optical and meteor head echo measurements using the Middle Atmosphere Alomar Radar System (MAARSY): Data collection and preliminary analysis. *Planetary and Space Science*, *141*, 25–34. doi: https://doi.org/10.1016/j.pss.2017.04.013

Brykina, I., & Egorova, L. (2023). On the ablation parameter in the problem of a meteor body entering the atmosphere. *Fluid Dynamics*, *58*(8), 1465–1471.

Campbell-Brown, M. D. (2019). Meteoroid structure and fragmentation. *Planetary and Space Science*, *169*, 1–7.

Campbell-Brown, M. D., Borovička, J., Brown, P., & Stokan, E. (2013). High-resolution modelling of meteoroid ablation. *Astronomy & Astrophysics*, *557*, A41.

Campbell-Brown, M. D., & Close, S. (2007). Meteoroid structure from radar head echoes. *Monthly Notices of the Royal Astronomical Society*, *382*(3), 1309–1316. doi: https://doi.org/10.1111/j.1365-2966.2007.12471.x

Čapek, D. (2014). Rotation of cometary meteoroids. *Astronomy & Astrophysics*, *568*, A39.

Ceplecha, Z., Borovička, J., Elford, W., ReVelle, D., Hawkes, R., Porubčan, V., & Šimek, M. (1998). Meteor phenomena and bodies. *Space Science Reviews*, *84*, 327–471. doi: https://doi.org/10.1023/A:1005069928850

Chau, J. L., Strelnikova, I., Schult, C., Oppenheim, M. M., Kelley, M. C., Stober, G., & Singer, W. (2014). Nonspecular meteor trails from non-

field-aligned irregularities: Can they be explained by presence of charged meteor dust? *Geophysical Research Letters*, *41*(10), 3336–3343. doi: https://doi.org/10.1002/2014GL059922

Chau, J. L., & Woodman, R. F. (2004). Observations of meteor-head echoes using the Jicamarca 50 MHz radar in interferometer mode. *Atmospheric Chemistry and Physics*, *4*, 511–521.

Close, S., Hunt, S. M., Minardi, M. J., & McKeen, F. M. (2000). Analysis of Perseid meteor head echo data collected using the Advanced Research Projects Agency Long-Range Tracking and Instrumentation Radar (ALTAIR). *Radio Science*, *35*(5), 1233–1240. doi: https://doi.org/10.1029/1999RS002277

Close, S., Kelley, M., Vertatschitsch, L., Colestock, P., Oppenheim, M. M., & Yee, J. (2011). Polarization and scattering of a long-duration meteor trail. *Journal of Geophysical Research: Space Physics*, *116*(A1), A01309. doi: https://doi.org/10.1029/2010JA015968

Close, S., Oppenheim, M. M., Durand, D., & Dyrud, L. (2005). A new method for determining meteoroid mass from head echo data. *Journal of Geophysical Research: Space Physics*, *110*, A09308. doi: https://doi.org/10.1029/2004JA010950

Close, S., Oppenheim, M. M., Hunt, S., & Coster, A. (2004). A technique for calculating meteor plasma density and meteoroid mass from radar head echo scattering. *Icarus*, *168*, 43–52. doi: https://doi.org/10.1016/j.icarus.2003.11.018

Close, S., Volz, R., Loveland, R., Macdonell, A., Colestock, P., Linscott, I., & Oppenheim, M. M. (2012). Determining meteoroid bulk densities using a plasma scattering model with high-power large-aperture radar data. *Icarus*, *221*, 300–309. doi: https://doi.org/10.1016/j.icarus.2012.07.033

Dimant, Y. S., & Oppenheim, M. M. (2017a). Formation of plasma around a small meteoroid: 1. kinetic theory. *Journal of Geophysical Research: Space Physics*, *122*(4), 4669–4696. doi: https://doi.org/10.1002/2017JA023960

Dimant, Y. S., & Oppenheim, M. M. (2017b). Formation of plasma around a small meteoroid: 2. implications for radar head echo. *Journal of Geophysical Research: Space Physics*, *122*(4), 4697–4711. doi: https://doi.org/10.1002/2017JA023963

Dyrud, L. P., & Janches, D. (2008). Modeling the meteor head echo using Arecibo radar observations. *Journal of Atmospheric and Solar-Terrestrial Physics*, *70*, 1621–1632. doi: https://doi.org/10.1016/j.jastp.2008.06.016

Dyrud, L. P., Ray, L., Oppenheim, M., Close, S., & Denney, K. (2005). Modelling high-power large-aperture radar meteor trails. *Journal of Atmospheric and Solar-Terrestrial Physics*, *67*, 1171–1177. doi: https://doi.org/10.1016/j.jastp.2005.06.016

Dyrud, L. P., Wilson, D., Boerve, S., Trulsen, J., Pecseli, H., Close, S., ... Lee, Y. (2008a). Plasma and electromagnetic simulations of meteor head echo radar reflections. *Earth, Moon and Planets*, *102*, 383–394. doi: https://doi.org/10.1007/s11038-007-9189-8

Dyrud, L. P., Wilson, D., Boerve, S., Trulsen, J., Pecseli, H., Close, S., ... Lee, Y. (2008b). Plasma and electromagnetic wave simulations of meteors. *Advances in Space Research*, *42*, 136–142. doi: https://doi.org/10.1016/j.asr.2007.03.048

Engelhardt, A. G., Phelps, A. V., & Risk, C. G. (1964). Determination of momentum transfer and inelastic collision cross sections for electrons in nitrogen using transport coefficients. *Phys. Rev.*, *135*, A1566–A1574. doi: https://doi.org/10.1103/PhysRev.135.A1566

Erickson, P. J., Lind, F. D., Wendelken, S. M., & Faubert, M. A. (2001). Meteor head echo observations using the Millstone Hill UHF incoherent scatter radar system. In *Proceedings of the meteoroids 2001 conference* (pp. 457–463).

Evans, J. V. (1965). Radio-echo studies of meteors at 68-centimeter wavelength. *Journal of Geophysical Research (1896–1977)*, *70*(21), 5395–5416. doi: https://

doi.org/10.1029/JZ070i021p05395

Frost, L. S., & Phelps, A. V. (1962). Rotational excitation and momentum transfer cross sections for electrons in H_2 and N_2 from transport coefficients. *Phys. Rev.*, *127*, 1621–1633. doi: https://doi.org/10.1103/PhysRev.127.1621

Garrett, H. B., & Close, S. (2013). Impact-induced ESD and EMI/EMP effects on spacecraft - a review. *IEEE Transactions on Plasma Science*, *41*(12), 3545–3557. doi: https://doi.org/10.1109/TPS.2013.2286181

Gurevich, A. (1978). *Nonlinear Phenomena in the Ionosphere.* New York/Heidelberg/Berlin: Springer-Verlag.

Guttormsen, G., Fletcher, A. C., & Oppenheim, M. M. (2020). Atomic-scale simulations of meteor ablation. *Journal of Geophysical Research: Space Physics*, *125*. doi: https://doi.org/10.1029/2020JA028229

Hedges, T., Ferguson, J., Lee, N., Elschot, S., Sugar, G., & Oppenheim, M. M. (2025). *Software and Results from Meteoroid Heat Transfer and Plasma Simulations Used to Investigate Anisotropy of Meteoroid Ablation* [dataset]. Stanford Digital Repository. doi: https://doi.org/10.25740/hm841hz7021

Hedges, T., Lee, N., & Elschot, S. (2022). Meteor head echo analyses from concurrent radar observations at AMISR Resolute Bay, Jicamarca, and Millstone Hill. *Journal of Geophysical Research: Space Physics*, *127*(10), e2022JA030709. doi: https://doi.org/10.1029/2022JA030709

Hedges, T., Lee, N., & Elschot, S. (2024). Meteor head echo detection at multiple high-power large-aperture radar facilities via a convolutional neural network trained on synthetic radar data. *Journal of Geophysical Research: Space Physics*, *129*(4), e2023JA032204. doi: https://doi.org/10.1029/2023JA032204

Janches, D., Dyrud, L. P., Broadley, S. L., & Plane, J. M. C. (2009). First observation of micrometeoroid differential ablation in the atmosphere. *Geophysical Research Letters*, *36*. doi: https://doi.org/10.1029/2009GL037389

Janches, D., Hocking, W., Pifko, S., Hormaechea, J. L., Fritts, D. C., Brunini, C., ... Samara, M. (2014). Interferometric meteor head echo observations using the Southern Argentina Agile Meteor Radar. *Journal of Geophysical Research: Space Physics*, *119*(3), 2269–2287. doi: https://doi.org/10.1002/2013JA019241

Jones, J., Jones, W., & Halliday, I. (1999). The head echo problem - a solution at last? In *Meteoroids 1998.*

Kelley, M. C., Pancoast, S., Close, S., & Wang, Z. (2012, 3). Analysis of electromagnetic and electrostatic effects of particle impacts on spacecraft. *Advances in Space Research*, *49*(6), 1029–1033. doi: https://doi.org/10.1016/j.asr.2011.12.023

Kozlovsky, A., Lukianova, R., & Lester, M. (2020). Occurrence and altitude of the long-lived nonspecular meteor trails during meteor showers at high latitudes. *Journal of Geophysical Research: Space Physics*, *125*. doi: https://doi.org/10.1029/2019JA027746

Lau, R., & Elschot, S. (2025). A curvature-based mechanism for the spontaneous emission of electromagnetic radiation at curved plasma–vacuum interfaces. *Physics of Plasmas*, *32*(1), 012107. doi: https://doi.org/10.1063/5.0250191

Lau, R., Lee, N., & Elschot, S. (2024). Spatial decay of electromagnetic waves from hypervelocity impact plasmas. *International Journal of Impact Engineering*, *187*, 104924. doi: https://doi.org/10.1016/j.ijimpeng.2024.104924

Li, A., & Close, S. (2016). Neutral density estimation derived from meteoroid measurements using high-power, large-aperture radar. *Journal of Geophysical Research*, *121*, 8023–8037. doi: https://doi.org/10.1002/2015JD024547

Li, Y., Galindo, F., Urbina, J., Zhou, Q., & Huang, T. (2022). Meteor detection with a new computer vision approach. *Radio Science*, *57*(10), e2022RS007515. doi: https://doi.org/10.1029/2022RS007515

Li, Y., Galindo, F., Urbina, J., Zhou, Q., & Huang, T. (2023). A machine learn-

ing algorithm to detect and analyze meteor echoes observed by the Jicamarca radar. *Remote Sensing*, *15*(16). doi: https://doi.org/10.3390/rs15164051

Li, Y., Zhou, Q., Scott, M., & Milla, M. (2020). A study on meteor head echo using a probabilistic detection model at Jicamarca. *Journal of Geophysical Research: Space Physics*, *125*(1), e2019JA027459. doi: https://doi.org/10.1029/2019JA027459

Limonta, L., Close, S., & Marshall, R. A. (2020). A technique for inferring lower thermospheric neutral density from meteoroid ablation. *Planetary and Space Science*, *180*. doi: https://doi.org/10.1016/j.pss.2019.104735

Longo, G. M., & Longo, S. (2018). Theoretical analysis of the atmospheric entry of sub-mm meteoroids of $Mg_xCa_{1-x}CO_3$ composition. *Icarus*, *310*, 194–202. doi: https://doi.org/10.1016/j.icarus.2017.12.001

Love, S., & Brownlee, D. (1991). Heating and thermal transformation of micrometeoroids entering the Earth's atmosphere. *Icarus*, *89*(1), 26–43. doi: https://doi.org/10.1016/0019-1035(91)90085-8

Marshall, R. A., Brown, P., & Close, S. (2017). Plasma distributions in meteor head echoes and implications for radar cross section interpretation. *Planetary and Space Science*, *143*, 203–208. doi: https://doi.org/10.1016/j.pss.2016.12.011

Marshall, R. A., & Close, S. (2015). An FDTD model of scattering from meteor head plasma. *Journal of Geophysical Research: Space Physics*, *120*, 5931–5942. doi: https://doi.org/10.1002/2015JA021238

Oppenheim, M. M., Dimant, Y., & Dyrud, L. P. (2008). Large-scale simulations of 2-D fully kinetic Farley-Buneman turbulence. *Annales Geophysicae*, *26*(3), 543–553. doi: https://doi.org/10.5194/angeo-26-543-2008

Oppenheim, M. M., & Dimant, Y. S. (2013). Kinetic simulations of 3-D Farley-Buneman turbulence and anomalous electron heating. *Journal of Geophysical Research: Space Physics*, *118*(3), 1306–1318. doi: https://doi.org/10.1002/jgra.50196

Oppenheim, M. M., & Dimant, Y. S. (2015). First 3-D simulations of meteor plasma dynamics and turbulence. *Geophysical Research Letters*, *42*, 681–687. doi: 10.1002/2014GL062411

Oppenheim, M. M., Vom Endt, A. F., & Dyrud, L. P. (2000). Electrodynamics of meteor trail evolution in the equatorial E-region ionosphere. *Geophysical Research Letters*, *27*(19), 3173–3176. doi: https://doi.org/10.1029/1999GL000013

Panka, P. A., Weryk, R. J., Bruzzone, J., Janches, D., Schult, C., Stober, G., & Hormaechea, J. (2021, 9). An improved method to measure head echoes using a meteor radar. *The Planetary Science Journal*, *2*(5), 197. doi: https://doi.org/10.3847/PSJ/ac22b2

Popova, O. (2004). Meteoroid ablation models. *Earth, Moon, and Planets*, *95*, 303–319.

Popova, O., Sidneva, S., Strelkov, A., & Shuvalov, V. (2001). Formation of disturbed area around fast meteor body. *Proceedings of the Meteoroids 2001 Conference*, 237–245.

Sam, A., Kumar, P., Fletcher, A. C., Crabtree, C., Lee, N., & Elschot, S. (2025). Nonlinear evolution, propagation, electron-trapping, and damping effects of ion-acoustic solitons using fully kinetic PIC simulations. *Physics of Plasmas*, *32*(2), 022103. doi: https://doi.org/10.1063/5.0249525

Sparks, J. J., Janches, D., Nicolls, M. J., & Heinselman, C. (2010). Determination of physical and radiant meteor properties using PFISR interferometry measurements of head echoes. *Journal of Atmospheric and Solar-Terrestrial Physics*, *72*(16), 1221–1230. doi: https://doi.org/10.1016/j.jastp.2010.08.004

Sugar, G., Marshall, R., Oppenheim, M. M., Dimant, Y. S., & Close, S. (2021). Simulation-derived radar cross sections of a new meteor head plasma distribution model. *Journal of Geophysical Research: Space Physics*, *126*(7),

e2021JA029171. doi: https://doi.org/10.1029/2021JA029171

Sugar, G., Oppenheim, M. M., Dimant, Y. S., & Close, S. (2018). Formation of plasma around a small meteoroid: Simulation and theory. *Journal of Geophysical Research: Space Physics*, *123*, 4080–4093. doi: https://doi.org/10.1002/2018JA025265

Sugar, G., Oppenheim, M. M., Dimant, Y. S., & Close, S. (2019). Formation of plasma around a small meteoroid: Electrostatic simulations. *Journal of Geophysical Research: Space Physics*, *124*, 3810–3826. doi: https://doi.org/10.1029/2018JA026434

Tárano, A. M., Wheeler, L. F., Close, S., & Mathias, D. L. (2019). Inference of meteoroid characteristics using a genetic algorithm. *Icarus*, *329*, 270–281. doi: https://doi.org/10.1016/j.icarus.2019.04.002

Tarnecki, L. K., Marshall, R. A., Stober, G., & Kero, J. (2021). Meteoroid mass estimation based on single-frequency radar cross section measurements. *Journal of Geophysical Research: Space Physics*, *126*(9), e2021JA029525. doi: https://doi.org/10.1029/2021JA029525

Virtanen, P., Gommers, R., Oliphant, T. E., Haberland, M., Reddy, T., Cournapeau, D., ... Scipy 1.0 Contributors (2020). SciPy 1.0: fundamental algorithms for scientific computing in Python. *Nature methods*, *17*(3), 261–272.

Volz, R., & Close, S. (2012). Inverse filtering of radar signals using compressed sensing with application to meteors. *Radio Science*, *47*, RS0N05. doi: https://doi.org/10.1029/2011RS004889

Vondrak, T., Plane, J. M. C., Broadley, S., & Janches, D. (2008). A chemical model of meteoric ablation. *Atmospheric Chemistry and Physics*, *8*(23), 7015–7031. doi: https://doi.org/10.5194/acp-8-7015-2008

Zalogin, G. N., & Kusov, A. L. (2016). The solution of a model problem of the atmospheric entry of a small meteoroid. *Cosmic Research*, *54*(2), 96–104. doi: https://doi.org/10.1134/S0010952516020088